Materials Advances

ROYAL SOCIETY OF CHEMISTRY

PAPER

View Article Online
View Journal | View Issue

Cite this: *Mater. Adv.*, 2026, 7, 2337

Enhancing the uniformity of $CuBi_2O_4$ thin films for photoelectrochemical (PEC) water splitting through a urea-modified ethylene glycol electrolyte

Xiuru Yang,[a] Mansour Alhabradi,[bc] Anurag Roy,[b] Manal Alruwaili,[bd] David Benson,[b] Hong Chang,[a] Xiaohong Li,[b] Asif Ali Tahir*[b] and Yanqiu Zhu*[a]

A $CuBi_2O_4$ photocathode with interconnected nanoparticle textured morphology has achieved a photocurrent density of −0.94 mA cm^{-2} at 0.52 V *vs.* RHE. It was successfully fabricated *via* electrodeposition using ethylene glycol (EG) containing a specific concentration of $Bi(NO_3)_3{\cdot}5H_2O$ and $CuCl_2{\cdot}2H_2O$ as the electrolyte, followed by 2 h of calcination at 550 °C. Using urea as a complexing agent in the EG electrolyte enhanced the photocurrent density of the $CuBi_2O_4$ photocathode. Adding 0.15 g of urea to the electrodeposition solution improved film uniformity, enhanced PEC water splitting efficiency, and achieved a photocurrent density of −1.44 mA cm^{-2} at 0.52 V *vs.* RHE. This value is higher than those of previously reported $CuBi_2O_4$ photocathodes, which typically exhibit photocurrent densities below −1.0 mA cm^{-2}. To understand the factors contributing to this enhanced PEC performance, this study investigated the effects of varying urea concentrations (0, 0.1, 0.15, and 0.2 g per 100 mL EG) on the crystallite domain size, morphology, surface roughness, light absorption, band gap, electronic band structure, and PEC performance. A mechanism was proposed to account for the long-term stability based on its inadequate valence band potential and irreversible degradation behaviour. This work provides insights for optimizing $CuBi_2O_4$ thin films to enhance their stability and efficiency in PEC water splitting applications.

Received 16th September 2025,
Accepted 21st December 2025

DOI: 10.1039/d5ma01065a

rsc.li/materials-advances

Introduction

Photoelectrochemical (PEC) water splitting, which can be used to directly convert solar energy to hydrogen, has been identified as a critical alternative for developing a more efficient, sustainable, and environmentally friendly future energy system. Efficient PEC hydrogen generation relies heavily on the development of suitable photocathodes. Materials such as Si,[1] GaAs,[1] CuO,[2] Cu_2O,[3] $LaFeO_3$,[4] $CuInS_2$,[5] $CuFeO_2$,[6] Sb_2Se_3,[7] InP,[8] and Cu_2ZnSnS_4[9] have been explored due to their conduction band potentials being more negative than the H^+/H_2 reduction potential ($E(H^+/H_2) = 0$ V *vs.* RHE),[10,11] enabling energy-efficient hydrogen evolution. Among p-type semiconductors, $CuBi_2O_4$ has attracted significant attention as a photocathode owing to its low bandgap energy (1.5–1.8 eV) and favorable band structure, which predicts a photocurrent density of 19–27 mA cm^{-2} under standard solar illumination (AM 1.5G, 100 mW cm^{-2}).[12,13] However, practical application of $CuBi_2O_4$ thin films is significantly hindered by their intrinsic limitations such as low charge carrier transfer kinetics, rapid recombination of photogenerated charge carriers, and susceptibility to photocorrosion. Achieving high-quality thin films with uniform thickness, controlled morphology, and strong adhesion to substrates remain essential for improving the overall performance of $CuBi_2O_4$ thin films.

Various techniques, including spin coating,[14,15] pulsed laser deposition (PLD),[16,17] physical vapor deposition (PVD) techniques (sputtering and electron beam evaporation),[18–20] doctor blade coating,[21,22] spray pyrolysis,[23,24] chemical bath deposition,[25,26] and electrodeposition,[27,28] have been used to fabricate $CuBi_2O_4$ thin films. Among these, electrodeposition is particularly attractive due to its low cost, mild operating temperature, and ability to produce adherent interfaces, making it highly suitable for the creation of durable thin films. However, non-uniform electrodeposition can reduce film quality and photocathode performance. To address these issues, various strategies have been explored, including adjusting the metal-ion concentration, implementing pH control

[a] *Faculty of Environment, Science and Economy, University of Exeter, Exeter EX4 4QF, UK*
[b] *Faculty of Environment, Science and Economy, University of Exeter, Penryn TR10 9FE, UK. E-mail: Y.Zhu@exeter.ac.uk*
[c] *Department of Physics, Faculty of Science, Majmaah University, Majmaah, 11952, Saudi Arabia*
[d] *Department of Physics, Faculty of Science, Jouf University, 2014, Sakaka 42421, Saudi Arabia*

through buffering, and adding organic additives during the deposition process. Nakabayashi *et al.* improved the uniformity of $CuBi_2O_4$ thin films by using tartrate ions to stabilize the Cu^{2+} and Bi^{3+} in solution. This stabilization enabled controlled co-deposition of CuO and Bi_2O_3 at a high anodic potential.[29] After annealing at 500 °C, the resulting $CuBi_2O_4$ thin films exhibited enhanced coverage, stronger adhesion, and better uniformity. Similarly, Hahn *et al.* prepared Cu–Bi electrodeposition baths by dissolving Bi^{3+} and Cu^{2+} in 10% nitric acid. This step was essential for fully dissolving bismuth nitrate and producing a homogeneous electrolyte, which is critical for consistent electrodeposition.[27] The homogeneous bath enabled effective cathodic co-deposition and subsequent annealing yield well-crystallized $CuBi_2O_4$ thin films. Citric acid has also been employed as a complexing agent in $CuBi_2O_4$ synthesis. By forming stable metal–ligand complexes, it regulates the release of metal ions during electrodeposition, thereby promoting uniform film growth.[30]

Urea is a small, inexpensive, and environmentally friendly molecule with strong hydrogen-bonding and coordination abilities.[31–33] Its $–NH_2$ group can donate hydrogen bonds while its carbonyl oxygen can accept them, enabling interactions with solvent molecules and metal ions.[31–33] These interactions tune the solvation environment, improve ion dissolution, and influence key solution properties such as ionic conductivity and viscosity, ultimately promoting uniform metal deposition and controlled thin-film growth.[31,34,35] Motivated by these advantages, this work investigates the effect of urea at varying concentrations (0, 0.1, 0.15, and 0.2 g per 100 mL of ethylene glycol, EG) on the synthesis of $CuBi_2O_4$ thin films on FTO glass. The resulting thin films are systematically characterized in terms of crystallite size, morphology features, surface roughness, electronic band structures, and PEC performance. Based on the observed enhancements, a potential mechanism involving charge separation and transfer is proposed to account for the enhancements in PEC performance.

Experimental procedures

Materials and chemicals

The following chemicals were purchased and utilised without additional purification: bismuth(III) nitrate pentahydrate ($Bi(NO_3)_3{\cdot}5H_2O$, 98%, Thermo Scientific Chemicals), copper(II) chloride dihydrate ($CuCl_2{\cdot}2H_2O$, 99 + %, ACS reagent, Thermo Scientific Chemicals), Sodium hydroxide (NaOH, 98%, extra pure, pellets, Acros Organics), and urea (CH_4N_2O, ultra-pure UPS grade, Melford). Ethylene glycol (EG, $C_2H_6O_2$, 99%, Thermo Scientific Chemicals) was used as the electrolyte for electrodeposition.

$CuBi_2O_4$ thin film preparation

A standard three-electrode system, consisting of a Pt counter electrode, an FTO working electrode, and an Ag/AgCl (4 M KCl) reference electrode, was used for the electrodeposition process. The FTO glass was electrically connected by placing copper tape on its edge with copper tape to ensure uniform current distribution when clipped with the Autolab tweezer during electrodeposition. A 100 mL EG solution comprising 6 mM Bi $(NO_3)_3{\cdot}5H_2O$, 3 mM $CuCl_2{\cdot}2H_2O$, and various amounts (0 g, 0.1 g, 0.15 g, and 0.2 g) of urea was utilised as the plating solution to create the Cu/Bi bimetallic films. The material was deposited by passing −0.06 C per cycle at a fixed potential of $E = -1.8$ V *versus* Ag/AgCl.[10] After six rounds of this cycle by accumulating a total charge of −0.36 C, the resulting Cu/Bi films were heated for 2 h at 550 °C in air with a ramping rate of 5 °C min^{-1} to produce the $CuBi_2O_4$ thin films. The samples were labelled as 0.1 g-urea-6C-9mM, 0.15 g-urea-6C-9mM and 0.2 g-urea-6C-9mM, respectively. As a reference, a sample generated using the same process but without adding urea into the EG electrolyte was labelled as 0 g-urea-6C-9mM.

PEC measurements

The Metrohm Autolab (PGSTAT302N) electrochemical workstation with a three-electrode compartment was used for all PEC analyses of the thin films. Platinum served as the counter electrode, Ag/AgCl (4 M KCl) as the reference electrode, and thin film as the working electrode, with 0.1 M NaOH at a pH of 12.8 as the electrolyte. A Newport 66 902, 300 W xenon lamp with an air mass (AM) of 1.5 was used to approximate a light intensity of 100 mW cm^{-2} (1 sun condition). The photocurrent density *vs.* $E_{Ag/AgCl}$ curves (*J–V* plots) were obtained by using the linear sweeping voltammetry (LSV) mode at a constant scan rate of 10 mV s^{-1} from −0.50 to 0.2 V *vs.* Ag/AgCl. At a bias potential of −0.45 V *vs.* Ag/AgCl, the electrochemical impedance spectroscopy (EIS) curves were recorded with a frequency range of 100 kHz to 0.1 Hz under a modulation amplitude of 10 mV. To compare with literature results, the experimental potential measured *versus* the Ag/AgCl reference electrode ($E_{Ag/AgCl}$) was converted to the potential *versus* the reversible hydrogen electrode (E_{RHE}) *via* the following Nernst eqn (1):[36,37]

$$E_{RHE} = E_{Ag/AgCl} + E^0_{Ag/AgCl} + 0.0591\ V \times pH\ (E^0_{Ag/AgCl} = 0.1976\ V\ vs.\ NHE\ at\ 25\ ^\circ C) \quad (1)$$

where NHE is the normal hydrogen electrode.

Characterization studies

A monochromatic Cu-Kα (λ = 0.154 nm) X-ray diffractometer in conjunction with a Bruker D8 Advance X-ray diffractometer (XRD) was used to identify the crystal structures and phases of the thin films. The high-resolution surface morphology was investigated utilizing an FEI Nova 600 Nanolab focused ion beam-scanning electron microscope (FIB-SEM). A Bruker Innova Atomic Force Microscope (AFM, USA) was also used to assess the surface morphology and roughness of the thin films in a chosen region of 10 × 10 μm^2, using RTESP-300 high quality etched silicon probes in a peak force tapping mode. NanoScope Analysis v1.7 software (Bruker, USA) was applied to analyse the acquired AFM images. A Thermo Fisher Scientific NEXSA spectrometer, equipped with a micro-focused monochromatic Al X-ray source (1486.7 eV) with an X-ray spot size of 400 × 200 μm, was used to perform the X-ray photoelectron spectroscopy (XPS) and ultraviolet photoelectron spectroscopy (UPS) analysis. The photoelectron energy shift was calibrated

using the C 1s electron at 284.8 eV as the reference point. A PerkinElmer UV-VIS-NIR lambda 1050 spectrophotometer was used to obtain the UV-visible diffuse reflectance spectra (DRS) of the thin films, and the Kubelka–Munk function was used to estimate the bandgap energy associated with each spectrum.

Results and discussion

The XRD patterns in Fig. 1a showed that the thin films—0 g-urea-6C-9mM, 0.1 g-urea-6C-9mM, 0.15 g-urea-6C-9mM and 0.2 g-urea-6C-9mM—exhibited similar diffraction features. Specifically, the peaks at 2θ degree of 20.8°, 27.9°, 29.6°, 30.6°, 32.4°, 33.2°, 34.1°, 37.4°, 46.6°, 52.9°, 53.3° and 55.6° are attributed to the (200), (211), (220), (002), (102), (310), (112), (202), (411), (213), (402), and (332) planes of tetragonal $CuBi_2O_4$ (PDF#48-1886).[38,39] In addition, five other peaks at 26.5°, 37.7°, 51.4°, 61.6°, and 65.5° are observed and ascribed to the underlying FTO substrate.[40] No additional peaks or noticeable shifts were detected upon the usage of the urea, indicating high phase purity of the $CuBi_2O_4$ thin films.

The crystallite size of the $CuBi_2O_4$ thin films was estimated based on the (211) facets using the Scherrer equation,[41] as presented in Fig. 1b, having values of 1137, 998, 730, and 997 Å for 0 g-urea-6C-9mM, 0.1 g-urea-6C-9mM, 0.15 g-urea-6C-9mM, and 0.2 g-urea-6C-9mM, respectively. The variation in crystallite size can be attributed to the supersaturation-controlled nucleation and growth kinetics.[42,43] Although all samples contain identical Bi^{3+} and Cu^{2+} in 100 mL EG, the effective instantaneous supersaturation at the electrode is modulated by urea content.[42,43] Urea coordinates with Cu^{2+}/Bi^{3+} and interacts with the solvent through hydrogen bonding, controlling the rate of ion release during electrodeposition.[31,32] With 0.15 g urea, this produces a sustained supersaturation, promoting high nucleation density and restricting individual crystallite growth, resulting in the smallest crystallite size (730 Å).[42,43] Without urea, rapid ion release generates a brief supersaturation spike; although the nucleation barrier is low during the spike, its short duration limits the number of nuclei, leading to large crystallites (1137 Å).[42,43] At higher urea content (0.2 g), increased viscosity and slower ion diffusion again reduce nucleation, allowing the crystallite to grow larger (997 Å).[42,43]

The surface morphologies of the $CuBi_2O_4$ thin films were examined using SEM, with representative low-magnification images shown in Fig. S3 and high-magnification images in Fig. 2. All $CuBi_2O_4$ thin films exhibit uneven and rough surface features, with some regions containing small nanoparticles, while in others the nanoparticles coalesce into larger branched structures, forming interconnected networks. These networks display irregular, coral-like morphologies reminiscent of finger coral, characterized by pronounced variations in particle size, spatial distribution, and height. The size differences of nanoparticles among the four $CuBi_2O_4$ thin films were estimated from the particle diameter distribution histograms shown in Fig. 2. Specifically, the average diameter of the sample without urea (0 g-urea-6C-9mM) is 0.15 μm, whilst being 0.21 and 0.17 μm, respectively, for 0.1 g-urea-6C-9mM and 0.2 g-urea-6C-9mM, the largest average diameter of 0.24 μm being achieved for sample 0.15 g-urea-6C-9mM. This behavior can be understood by combining classical nucleation and growth with non-classical aggregation mechanisms:[42,43] small crystallites with high surface energy tend to aggregate, forming larger particles. With 0.15 g urea, moderated ion release sustains supersaturation, generating many small crystallites that aggregate in a controlled manner, producing well-packed particles and uniform films. Without or with excess urea, nucleation is limited and aggregation is slowed, resulting in less uniform particles. The low-resolution SEM images in Fig. S3 further highlight the differences in coral-like interconnected networks distribution, with the urea-containing thin films, especially 0.1 g-urea-6C-9mM and 0.15 g-urea-6C-9mM thin films, showing the most pronounced branched structures.

The cross-sectional SEM images in Fig. 3 reveal that all $CuBi_2O_4$ thin films are composed of nanoparticle aggregates coalesced into porous, irregular networks. Their vertical height of these branched regions varies, and the mean thickness was

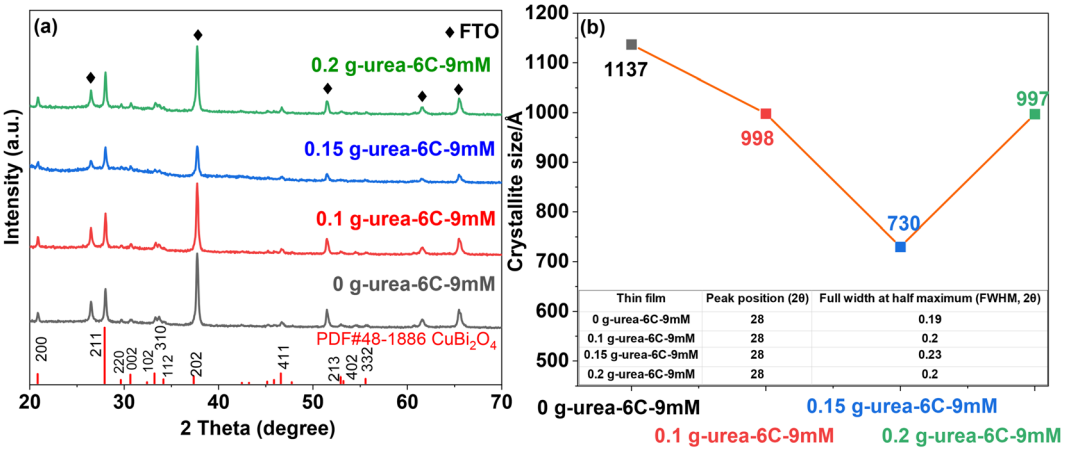

Fig. 1 (a) XRD patterns and (b) corresponding crystallite size of different $CuBi_2O_4$ thin films deposited on an FTO substrate.

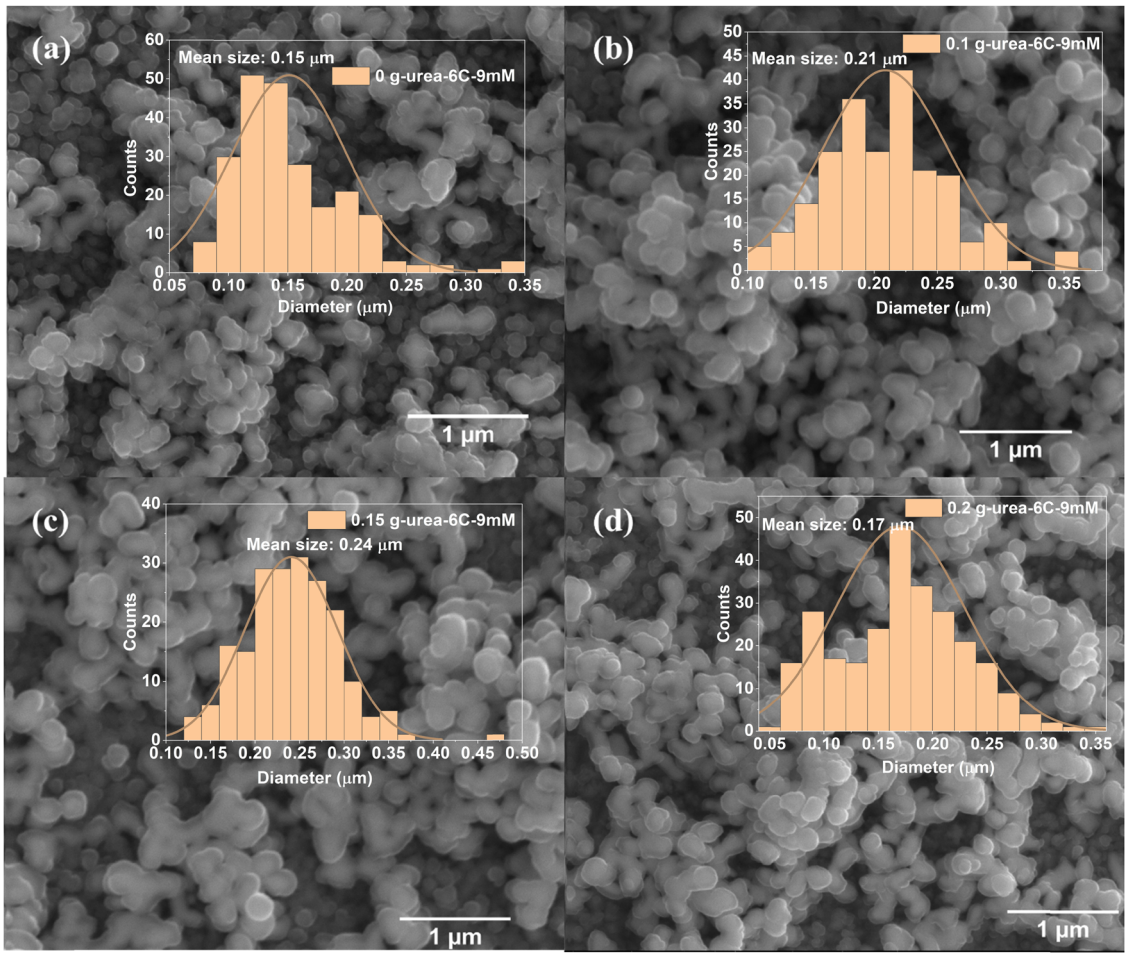

Fig. 2 SEM images of the top view and particle size distribution histograms of the resulting $CuBi_2O_4$ thin films on FTO substrates: (a) 0 g-urea-6C-9mM; (b) 0.1 g-urea-6C-9mM; (c) 0.15 g-urea-6C-9mM; and (d) 0.2 g-urea-6C-9mM.

determined from the thickness histogram in Fig. 3. The thin film prepared under urea-free conditions (0 g-urea-6C-9mM) exhibits a moderately compact structure with a mean thickness of ~1.1 μm. In contrast, films deposited from urea-containing electrolytes display increased thicknesses of ~1.5 μm (0.1 g-urea-6C-9mM), ~1.4 μm (0.15 g-urea-6C-9mM), and ~1.5 μm (0.2 g-urea-6C-9mM). These results show that urea promotes vertical growth by moderating ion release during electrodeposition, which enhances nucleation and aggregation along the vertical direction, leading to thicker, more pronounced branched structures. EDS spectra displayed in Fig. S4 show that Cu, Bi, O, Sn, Si, and the coated C are present in all thin films. The Cu/Bi atomic ratios of all samples, derived from EDS analysis, are 3.09 : 6.39 for 0 g-urea-6 C-9 mM, 3.49 : 7.62 for 0.1 g-urea-6C-9mM, 9.86 : 19.48 for 0.15 g-urea-6C-9mM, and 0.97 : 1.94 for 0.2 g-urea-6C-9mM. These values correspond closely to a Cu : Bi ratio of approximately 1 : 2, consistent with the stoichiometric composition of $CuBi_2O_4$. This result demonstrates the successful synthesis of $CuBi_2O_4$ thin films, which is consistent with the XRD analysis.

Three-dimensional (3D) perspective topographical pictures displayed in Fig. 4 present the vertical height variations caused by the bumps, pits, or other surface irregularities. The topologies of all the $CuBi_2O_4$ thin films demonstrate non-uniform growth, characterized by regions that develop laterally large and vertically tall features, while other areas exhibit minimal growth. Specifically, thin films of 0.1 g-urea-6C-9mM and 0.15 g-urea-6C-9mM show more uniform distributions of laterally large and vertically tall features compared with thin films 0 g-urea-6C-9mM and 0.2 g-urea-6C-9mM. The two-dimensional (2D) views, showing the height signals along the given section lines, the corresponding mean roughness (R_a), the maximum height (R_{max}) values, and other related parameters, are presented in Fig. S5. Here R_{max} is defined as the height difference between the highest and lowest points on the cross-sectional profile relative to the centre line over the length of the profile. The variations in the R_{max} values indicate the non-uniform topology features of the thin films. The surface average R_a values of the $CuBi_2O_4$ thin films are 181.1 nm for sample 0 g-urea-6C-9mM, 174.9 nm for sample 0.1 g-urea-6C-9mM, sample 0.15 g-urea-6C-9mM for 154.2 nm, and 185.1 nm for 0.2 g-urea-6C-9mM (Fig. S5), indicating a more uniform surface for samples 0.1 g-urea-6C-9mM and 0.15 g-urea-6C-9mM.

According to the XPS survey scan results shown in Fig. S6, both samples have similar entire spectra with Cu 2p, Bi 4f, and O 1s peaks. Fig. 5a reveals the high-resolution Bi 4f spectra of

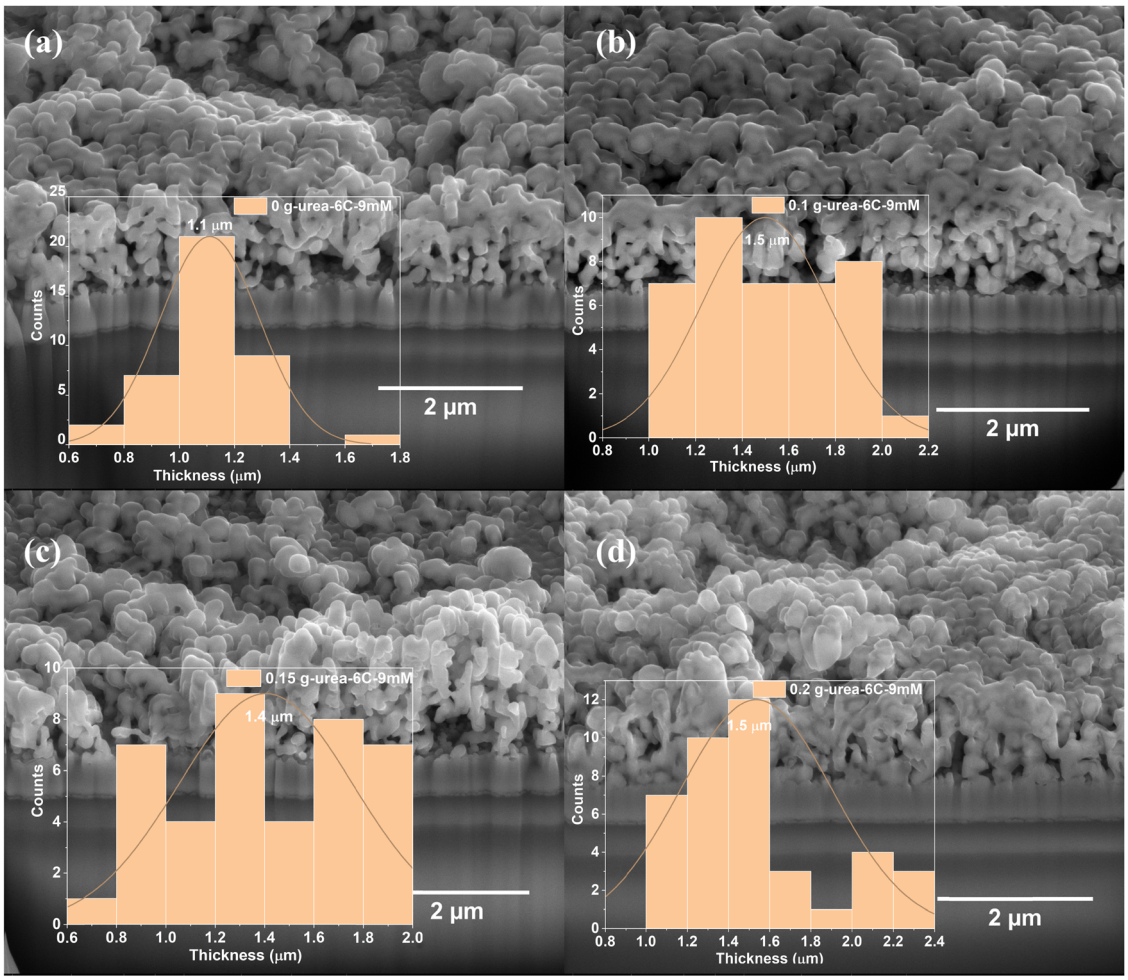

Fig. 3 SEM images of cross-section views and thickness histograms of the resulting $CuBi_2O_4$ thin films on FTO substrates: (a) 0 g-urea-6C-9mM; (b) 0.1 g-urea-6C-9mM; (c) 0.15 g-urea-6C-9mM; and (d) 0.2 g-urea-6C-9mM.

samples 0 g-urea-6C-9mM and 0.15 g-urea-6C-9mM. The binding energies at 158.6 and 163.9 eV are responsible for the typical spin–orbit split Bi $4f_{7/2}$ and Bi $4f_{5/2}$ peaks, respectively, which are brought on by the Bi^{3+} component in both samples.[44,45] The small peaks fitted at lower binding energies of 162.2 and 156.9 eV are attributed to residual metallic Bi on the surface of the $CuBi_2O_4$ lattice.[46,47] In Fig. 5b, the raw data exhibit four peaks: a doublet for Cu 2p and two additional shake-up peaks. These shake-up peaks are attributed to a strong interaction of the final states, involving charge transfer from O 2p band to the Cu 3d band.[48,49] Cu 2p spectra are typically featured by focusing on the Cu $2p_{3/2}$ peak and the lower binding energy shake-up peak, owing to their distinctive spectral features that allow for reliable fitting. Peaks with binding energies of 933.9 and 932.3 eV, fitted from the Cu $2p_{3/2}$ peak, are attributed to the Cu^{2+} in the $CuBi_2O_4$ lattice and Cu^{+} species, respectively.[44,49] Peaks located at 943.7 and 941.2 eV, obtained from the lower binding energy shake-up peak, further suggest the coexistence of these Cu^{2+} and Cu^{+} species within the $CuBi_2O_4$ thin films. The peak area ratios of Bi^{3+} and Bi (99 : 1), as well as those of Cu^{2+} and Cu^{+} (8 : 2), in the 0.15 g-urea-6C-9mM thin film and 0 g-urea-6C-9mM thin film, are maintained without significant change. This indicates that the addition of urea into the electrolyte during the electrodeposition process does not significantly affect the chemical composition and the chemical states of the $CuBi_2O_4$ thin film. To further confirm the chemical states and quantify the surface concentration of Cu species in the $CuBi_2O_4$ thin film, the Cu LM2 Auger spectra were analysed. As depicted in Fig. 5c, the Cu LM2 Auger electron spectra show peaks corresponding to the lattice Cu^{2+} (blue peaks) and the low-valence Cu^{+} species (red peaks).[50,51] This finding is consistent with the results obtained from the Cu 2p spectra. The O 1s spectra (Fig. 5d) for both $CuBi_2O_4$ samples were fitted into three distinct peaks at binding energies of approximately 529.4, 530.5, and 531.4 eV. These peaks are attributed to lattice oxygen (O_L),[50–52] surface hydroxyl group,[50,51] and absorbed water species, respectively. The presence of surface hydroxyl groups in $CuBi_2O_4$ is commonly associated with surface oxygen environments influenced by the coexistence of Cu^{2+}/Cu^{+} states, as observed in the Cu LM2 Auger spectra. The O_L peak area ratios for $CuBi_2O_4$ thin films of 0 g-urea-6C-9mM and 0.15 g-urea-6C-9mM are 49.5% and 47.2%, respectively, while the surface

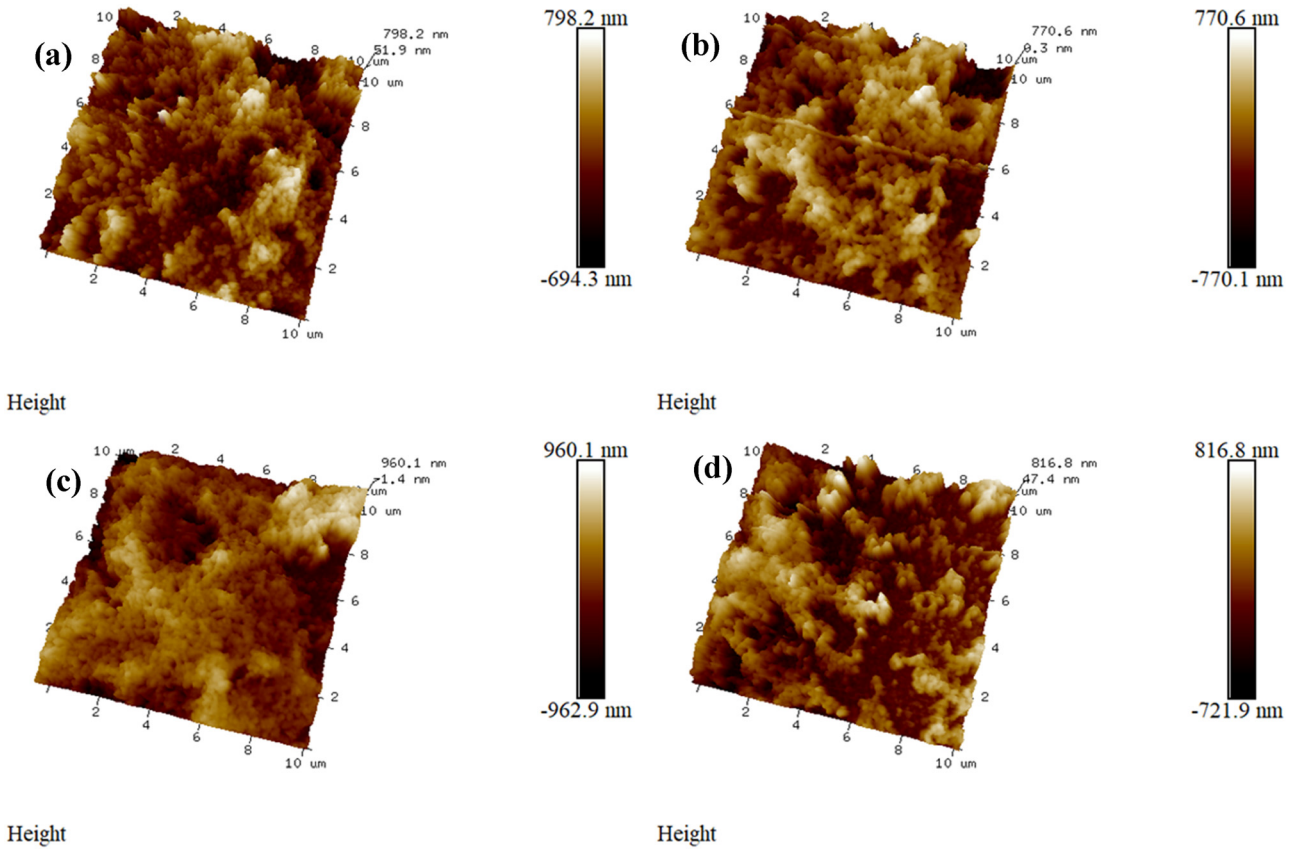

Fig. 4 AFM 3D perspectives of (a) 0 g-urea-6C-9mM, (b) 0.1 g-urea-6C-9mM, (c) 0.15 g-urea-6C-9mM, and (d) 0.2 g-urea-6C-9mM.

hydroxyl species for these two $CuBi_2O_4$ thin films are 39.3% and 42.1%, respectively. This variation may be attributed to the different distribution of aggregated, finger coral-like structures on the surface of the thin films.

The UV-visible absorbance spectra (Fig. 6a) exhibit strong visible-light absorptions in all thin films. The incident light absorbances of the $CuBi_2O_4$ thin films, 0.15 g-urea-6C-9mM and 0.2 g-urea-6C-9mM, are higher compared with those of 0 g-urea-6C-9mM and 0.1 g-urea-6C-9mM $CuBi_2O_4$. Slight red shifts can be observed upon introducing 0.15 g and 0.2 g urea into the electrodeposition process. This increase in optical absorption and reduction in reflectance (Fig. 6b, inset) are attributed to the varying surface topographical features induced by the urea. Fig. 6b presents the direct transition band gap values for the samples—1.88 eV for sample 0 g-urea-6C-9mM, 1.89 eV for sample 0.1 g-urea-6C-9mM, 1.87 eV for sample 0.15 g-urea-6C-9mM, and 1.86 eV for sample 0.2 g-urea-6C-9mM. These values are consistent with those reported in previous studies.[13]

Mott–Schottky measurements are utilized at 1 kHz in 0.1 M NaOH solution in dark conditions, to estimate the flat band potential (E_{fb}) and the hole density (N_A) of the $CuBi_2O_4$ thin films. The Mott–Schottky plots depicted in Fig. 7a were obtained from the following eqn (2):[54]

$$\frac{1}{C^2} = \frac{2}{A^2 e\varepsilon\varepsilon_0 N_A}\left(-E + E_{fb} - \frac{KT}{e}\right) \quad (2)$$

where the parameters C, A, E_{fb}, N_A, ε, ε_0, and E correspond to the capacitance, the electrode surface area (1×10^{-4} m^2), the flat-band potential, the acceptor density, the relative permittivity (dielectric constant) of 80 as reported previously,[54,55] the permittivity of free space (8.854×10^{-12} F m^{-1}),[36] and the applied potential, respectively.[54] As shown in Fig. 7a, the corresponding values of the slope and hole densities of the $CuBi_2O_4$ thin films were calculated and are listed in Table 1.[12] All the regression lines exhibit negative slopes, indicating that the samples are p-type semiconductors.[38] Comparison of the N_A values indicates that all samples exhibit hole densities of the same order of magnitude. Sample 0 g-urea-6 C-9 mM shows the highest hole density, likely due to the transition from Cu^+ to Cu^{2+}, which releases electrons and thereby enhances the hole density. The flat band potentials of the $CuBi_2O_4$ thin films are 1.41 V *vs.* RHE for samples 0 g-urea-6C-9mM and 0.1 g-urea-6C-9mM, and 1.40 V *vs.* RHE for sample 0.15 g-urea-6C-9mM and sample 0.2 g-urea-6C-9mM, respectively. In p-type semiconductors, the flat band potential is approximately aligned with the energy level near the valence band edge.[56] The potential of the conduction band can be determined based on the following eqn (3).[57]

$$E_c = E_v - E_g \quad (3)$$

The potentials of both the conduction and valence band positions relative to the water redox potential were constructed

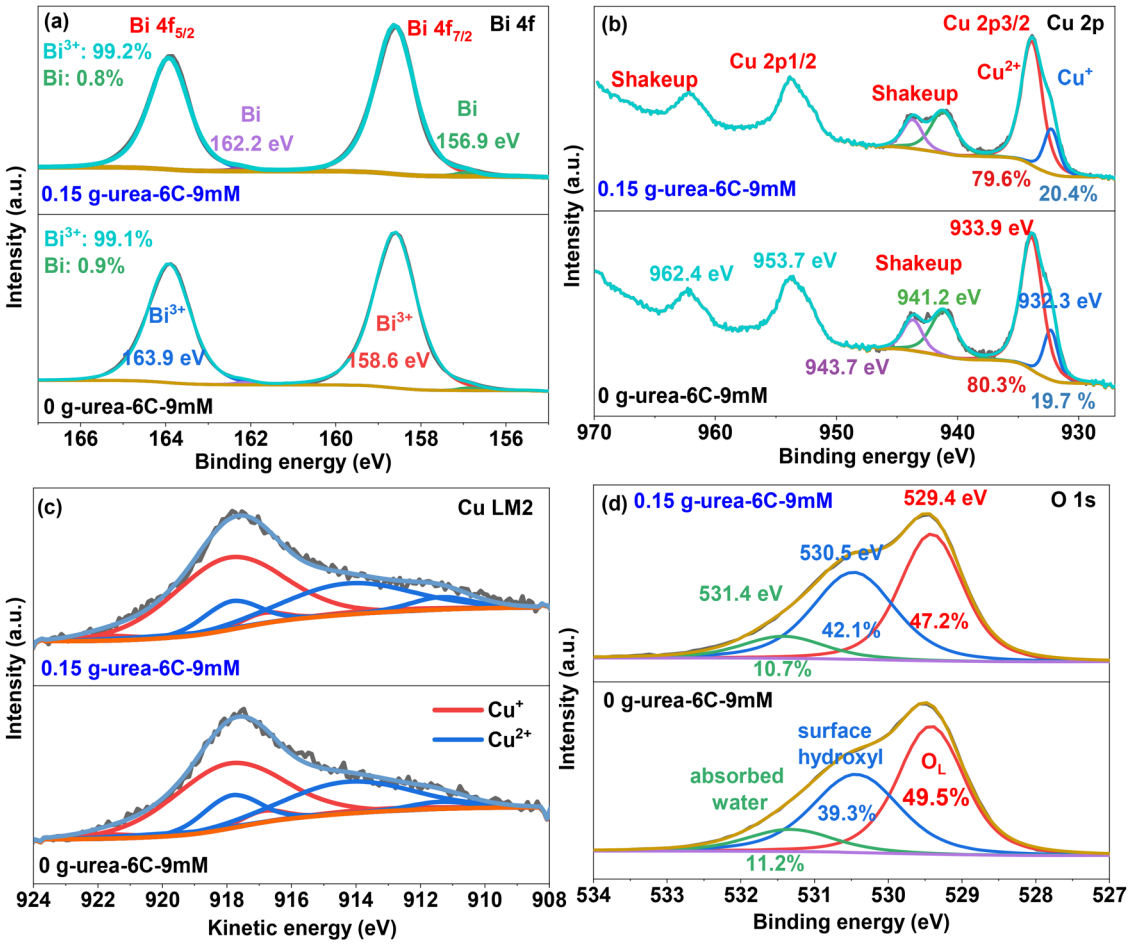

Fig. 5 XPS spectra of prepared $CuBi_2O_4$ thin films: 0 g-urea-6C-9mM and 0.15 g-urea-6C-9mM. (a) Bi 4f, (b) Cu 2p, (c), Cu LM2, and (d) O 1s.

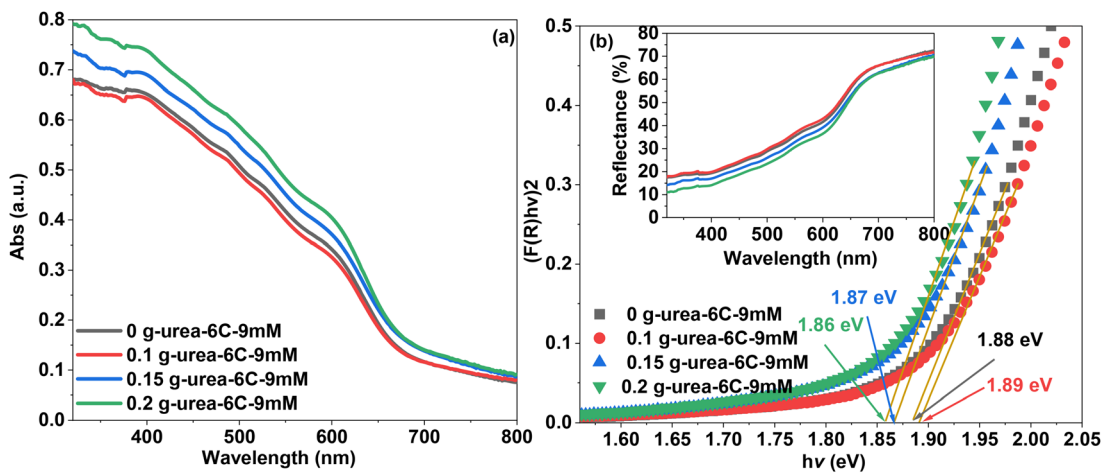

Fig. 6 (a) UV-visible absorbance spectra of the $CuBi_2O_4$ thin films and (b) the corresponding predicted band gap values from the Kubelka–Munk function,[53] with the UV-visible diffuse reflectance spectra (DRS) shown in the inset.

and illustrated in Fig. 7b. The valence band potentials of all the thin films at pH 12.8 are above 1.98 V *vs.* RHE (corresponding to 1.23 V *vs.* RHE at pH 0), while the conduction band potentials are above 0.75 V *vs.* RHE (corresponding to 0 V *vs.* RHE at pH 0).[58] Therefore, the $CuBi_2O_4$ thin films demonstrate the capability to perform the hydrogen evolution reaction under a pH of 12.8. Additionally, the band edge positions differ by only 10 mV, which is within the range of experimental error

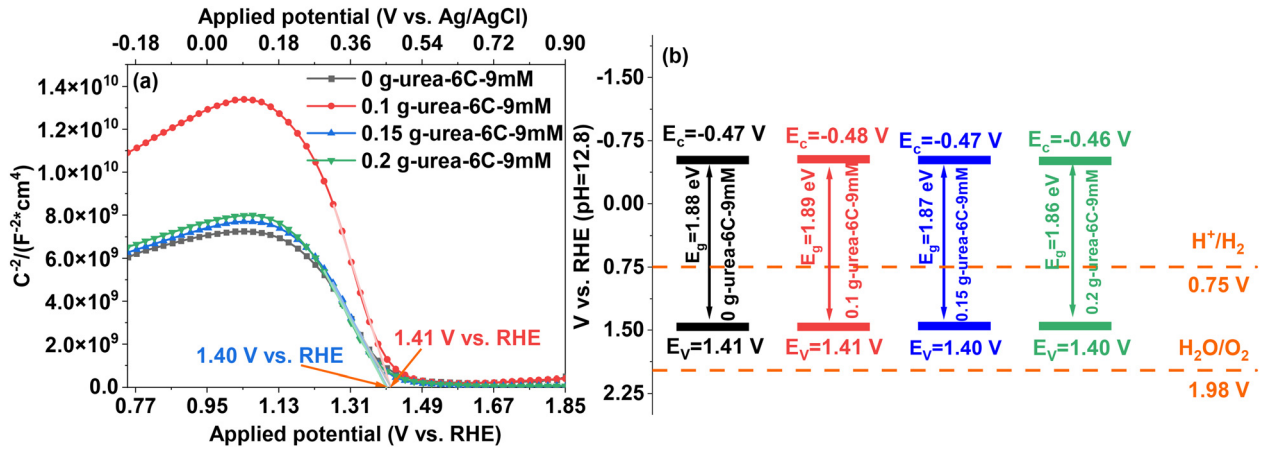

Fig. 7 Mott–Schottky plots (a) and (b) the estimated band structures of the $CuBi_2O_4$ thin films.

Table 1 Band edge potential position, Mott–Schottky slope values, and corresponding hole densities

Thin film	Conduction band potential (V *vs.* RHE)	Valence band potential (V *vs.* RHE)	Value of the slope	N_A (cm^{-3})
0 g-urea-6C-9mM	−0.47	1.41	-3.18×10^{10}	5.54×10^{19}
0.1 g-urea-6C-9mM	−0.48	1.41	-5.94×10^{10}	2.97×10^{19}
0.15 g-urea-6C-9mM	−0.47	1.40	-3.57×10^{10}	4.94×10^{19}
0.2 g-urea-6C-9mM	−0.46	1.40	-3.46×10^{10}	5.09×10^{19}

and would not significantly affect the overall band structure. The ultraviolet photoelectron spectroscopic (UPS) analysis using a He(I) laser ($h\nu$ = 21.22 eV) as the incident light was utilized to determine the work functions of the $CuBi_2O_4$ thin films. As illustrated in Fig. S7, the work functions for samples 0 g-urea-6C-9mM and 0.15 g-urea-6C-9mM are 5.03 eV and 5.21 eV, respectively. Therefore, the energy required to extract electrons from the materials differs by a maximum of 0.2 eV, which is quite similar and might not be enough to affect the PEC water splitting performance.

The *J–V* and Nyquist plots are displayed in Fig. 8, which were obtained from linear sweeping voltammetry (LSV) and frequency response analyser (FRA) impedance potentiostatic mode, respectively, for the investigation of the PEC performance of the $CuBi_2O_4$ thin films. In Fig. 8a, sample 0 g-urea-6C-9mM exhibits the highest photocurrent density of −0.94 mA cm^{-2} at 0.52 V *vs.* RHE, whilst the photocurrent density was further improved after the introduction of urea during the electrodeposition process, reaching −1.04 and −1.44 mA cm^{-2} for the 0.1 and 0.15 g urea samples, which is higher than previously published values (Table S2). Further increasing the amount of urea to 0.2 g led to a decreased photocurrent density of −0.99 mA cm^{-2}, which is still greater than that of sample 0 g-urea-6C-9mM. Therefore, the charge separation and transfer

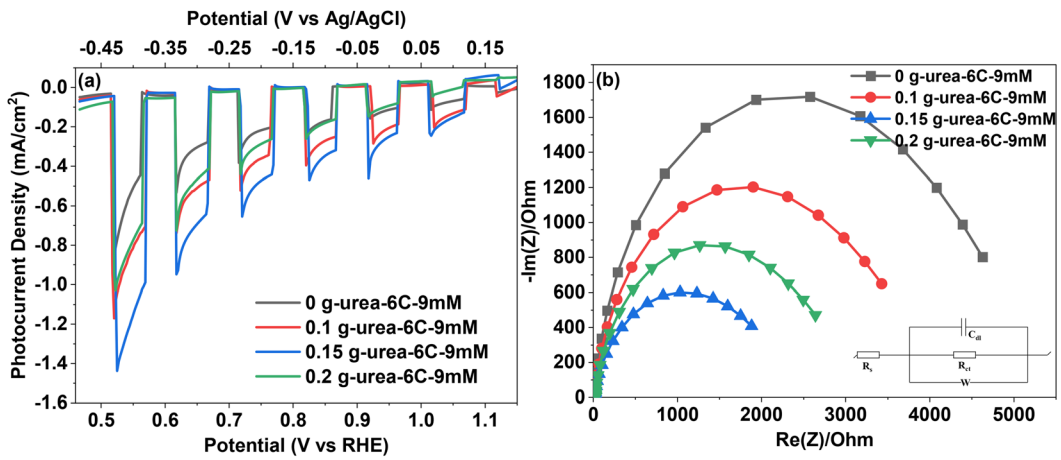

Fig. 8 (a) Photocurrent density-potential *vs.* RHE or Ag/AgCl (*J–V*) plots under chopped illumination conditions, (b) ESI Nyquist plots obtained at −0.45 V *vs.* Ag/AgCl under one sun simulated light illumination.

efficiencies have been improved. The Nyquist spectra (Fig. 8b) fitted *via* the following equivalent circuit inserted in the Fig. 8b are applied to investigate the charge-transfer resistance of the $CuBi_2O_4$ thin films. R_s represents the intercept of the semicircle with the real axis (Re(Z)) at low frequency, indicating the resistance of the electrolyte solution and any inherent resistance of the setup. The diameter of the semicircle in the Nyquist plot is utilized to determine the charge transfer resistance (R_{ct}) at the interface of the $CuBi_2O_4$ thin film and FTO glass. The double-layer capacitance (C_{dl}) represents the capacitive behaviour at the interface, while the Warburg impedance (W) indicates the influence of the diffusion processes on the impedance response in combination with the double-layer capacitance. According to Fig. 8b and Table 2, sample 0.15 g-urea-6C-9mM, which exhibits the smallest semicircle diameter, has the lowest charge transfer resistances (R_{ct}) with a value of 2430 Ω. This is followed by sample 0.2 g-urea-6C-9mM (R_{ct} = 3193 Ω), and sample 0.1 g-urea-6C-9mM (R_{ct} = 4169 Ω), whilst the urea-free reference $CuBi_2O_4$ thin film exhibits the highest charge transfer resistance of 5441 Ω. Therefore, the charge transfer efficiencies of the $CuBi_2O_4$ thin films are ranked as follows: 0.15 g-urea-6C-9mM > 0.2 g-urea-6C-9mM > 0.1 g-urea-6C-9mM > 0 g-urea-6C-9mM under the bias of 0.52 V *vs.* RHE. The C_{dl} values, however, exhibit an opposite trend, with the 0.15 g-urea-6C-9mM thin film showing the highest C_{dl} value. This implies a larger area for charge separation, potentially enhancing the PEC performance. The observed decrease in charge transfer resistance, coupled with the increased C_{dl}, indicates an improved efficiency in utilizing photogenerated charges for these thin films.

The stability of the $CuBi_2O_4$ thin films has been investigated using *I–t* curves measured through chronoamperometry under continuous solar light illumination for 2 h at 0.52 V *vs.* RHE. Thin film 0.15 g-urea-6C-9mM, which exhibits the highest photocurrent density, was used to investigate the stability performance in comparison to thin film 0 g-urea-6C-9mM. As shown in Fig. S8, both thin films showed poor PEC stabilities. Specifically, initial sharp drops in photocurrent density were observed within approximately 10 seconds. After 100 seconds of continuous illumination, both films reached their steady-state photocurrents, with sample 0.15 g-urea-6C-9mM exhibiting approximately −0.27 mA cm^{-2}, which is about 42% higher than the reference (−0.19 mA cm^{-2}).

The variations in PEC performance (photocurrent density and photostability) of the $CuBi_2O_4$ thin films can be primarily attributed to the urea-induced morphological differences. Examination of the charge–time curves (Fig. S9) recorded during electrodeposition reveals that the presence of urea slows the deposition process under the same applied charges. This effect arises from the coordination of urea with Cu^{2+} and Bi^{3+} ions, which stabilizes them in solution and maintains a steady concentration of electroactive species.[59,60] This behavior further supports the sustained-supersaturation condition proposed earlier, which governs both the nucleation rate and subsequent particle aggregation. Under the influence of urea, the resulting more continuous particle networks and slightly increased film thickness provide more efficient charge-transport pathways and reduce recombination at interparticle boundaries, accounting for the higher photocurrent densities of the urea-assisted thin films. Moreover, the improved structural coherence and uniformity help to moderate photocorrosion, explaining the modest enhancement in stability compared to the referent thin film (0 g-urea-6C-9mM).

Based on above analyses, a possible charge separation and transfer mechanism has been proposed to explain the improved PEC water splitting performance. As illustrated in Fig. 9, under solar light illumination, the $CuBi_2O_4$ thin film generates photocarriers after absorbing light with energy greater than its band gap. A built-in electric field separates the photo-generated electrons and holes. Ideally, the electrons will transfer to the surface of the $CuBi_2O_4$ thin film to participate in the reduction reaction eqn (4):[61]

$$4H_2O + 4e^- \rightarrow 2H_2 + 4^-OH \quad (4)$$

Meanwhile, the Pt counter electrode serves as the site for the oxidation reaction eqn (5):[61]

$$4^-OH \rightarrow O_2 + 2H_2O + 4e^- \quad (5)$$

The generated electrons at the counter electrode flow through the external circuit back to the $CuBi_2O_4$ thin film, completing the electrical circuit. However, an undesirable photocorrosion reaction occurs within the $CuBi_2O_4$ thin film due to the insufficiently anodic valence band potential of the synthesized $CuBi_2O_4$ photocathode (1.4 V *vs.* RHE at pH 12.8). This thermodynamic limitation prevents the efficient oxygen evolution reaction (OER), leading to

Table 2 Parameters: R_s, R_{ct}, C_{dl}, and W obtained from the fitted Nyquist plots of the $CuBi_2O_4$ thin films

	0 g-urea-6C-9mM	0.1 g-urea-C-9mM	0.15 g-urea-6C-9mM	0.2 g-urea-6C-9mM
R_s	26.22 Ω	23.06 Ω	20.75 Ω	25.31 Ω
R_{ct}	5441 Ω	4169 Ω	2430 Ω	3193 Ω
C_{dl}	15.26 μF	16.58 μF	18.29 μF	15.25 μF
W	14 593 Ω $s^{-0.5}$	9099 Ω $s^{-0.5}$	3925 Ω $s^{-0.5}$	6932 Ω $s^{-0.5}$

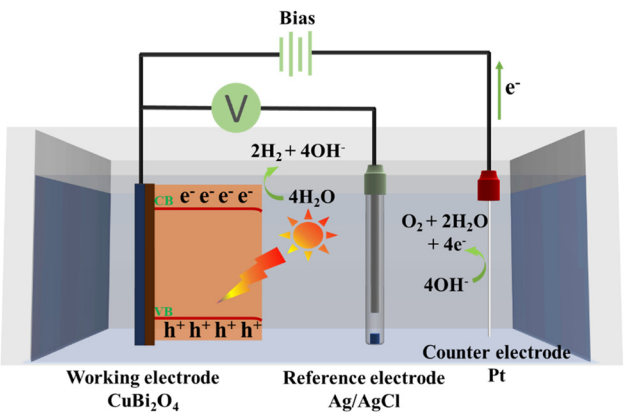

Fig. 9 Schematic illustration of the electronic transfer under the possible mechanism.

the photogenerated holes oxidizing the $CuBi_2O_4$ lattice and degrading the Cu–O–Bi framework into CuO and Bi_2O_3 rather than driving water oxidation (1.98 V *vs.* RHE at pH 12.8).[62–64] Furthermore, in an alkaline electrolyte, Bi^{3+} within the $CuBi_2O_4$ lattice reacts with hydroxide ions to form soluble hydroxo complexes,[62] leading to the bismuth leaching effect and structural destabilization. Simultaneously, Cu^+ species undergo the following disproportionation eqn (6):[63]

$$2Cu^+ \rightarrow Cu^{2+} + Cu^0 \quad (6)$$

where the resulting Cu^{2+} species react with hydroxide ions to form hydroxy complexes,[63] which further accelerates the lattice degradation. The residual photocurrent remains due to the presence of surviving $CuBi_2O_4$ domains and the photoactivity of the secondary phases.

Conclusions

This work successfully developed a $CuBi_2O_4$ photocathode with an interconnected nanoparticle textured morphology for PEC water splitting. AFM characterization showed that the $CuBi_2O_4$ thin film prepared with 0.15 g urea per 100 mL of EG exhibited the lowest surface roughness and best uniformity compared with thin films prepared with other urea concentrations. XPS analyses revealed that the element composition and chemical states, as well as the electronic band structures observed through electrochemical characterization, remained largely unchanged. This indicated that the variations of urea in the EG electrolyte primarily contributed to the physical differences, such as crystallite size, uniformity and thickness, rather than affecting the chemical performance. Durability tests demonstrated that, after 100 seconds of continuous illumination, the 0.15 g-urea-6C-9mM $CuBi_2O_4$ thin film stabilized at approximately -0.27 mA cm^{-2}, while the 0 g-urea-6C-9mM $CuBi_2O_4$ thin film stabilized at -0.19 mA cm^{-2}. This represents a 42% enhancement in stability for the 0.15 g-urea-6C-9mM $CuBi_2O_4$ thin film, which is attributed to its more uniform morphology. These findings underscore the introduction of urea into the EG electrolyte enhances the uniformity and performance of $CuBi_2O_4$ thin film, thereby improving their effectiveness in PEC water splitting applications.

Conflicts of interest

The authors declare that they have no known competing financial interests or personal relationships that could have appeared to influence the work reported in this paper.

Data availability

The data supporting this study, including XRD patterns, *J–V* curves, low-resolution SEM images, EDS spectra, AFM two-dimensional topographies and surface roughness profiles, XPS survey scan and C 1s spectra, UPS spectra, *I–t* stability curves, charge (C) *vs.* time (S) curves from electrodeposition and photocurrent density comparisons of the 0.15 g-urea-6C-9mM $CuBi_2O_4$ thin film with previously reported $CuBi_2O_4$ thin films, are available in the supplementary information (SI). See DOI: https://doi.org/10.1039/d5ma01065a.

Acknowledgements

A. A. Tahir and Y. Zhu acknowledge the Engineering and Physical Sciences Research Council (EPSRC), UK, under research grant numbers EP/T025875/1 and EP/V049046/1. Author X. Yang would like to acknowledge the financial support from the University of Exeter-China Scholarship Council PhD Scholarship. The authors would also like to thank Dr Shaoliang Guan of the University of Cardiff for his efforts towards XPS equipment support. For the purpose of open access, the authors have applied a Creative Commons Attribution (CC BY) licence to any Author Accepted Manuscript version arising from this submission.

References

1 Y. H. Lee, J. Kim and J. Oh, *ACS Appl. Mater. Interfaces*, 2018, **10**, 33230–33237, DOI: 10.1021/acsami.8b10943.
2 S. Masudy-Panah, R. S. Moakhar, C. S. Chua, A. Kushwaha, T. I. Wong and G. K. Dalapati, *RSC Adv.*, 2016, **6**, 29383–29390, DOI: 10.1039/c6ra03383k.
3 J. Luo, L. Steier, M.-K. Son, M. Schreier, M. T. Mayer and M. Grätzel, *Nano Lett.*, 2016, **16**, 1848–1857, DOI: 10.1021/acs.nanolett.5b04929.
4 G. S. Pawar, A. Elikkottil, S. Seetha, K. S. Reddy, B. Pesala, A. A. Tahir and T. K. Mallick, *ACS Appl. Energy Mater.*, 2018, **1**, 3449–3456, DOI: 10.1021/acsaem.8b00628.
5 Q. Cai, Z. Liu, C. Ma, Z. Tong and C. Han, *J. Mater. Sci.: Mater. Electron.*, 2018, **29**, 20629–20638, DOI: 10.1007/s10854-018-0201-z.
6 R.-P. Li, S.-M. Yu and Z.-Y. Zhao, *Mater. Chem. Phys.*, 2024, **311**, 128582, DOI: 10.1016/j.matchemphys.2023.128582.
7 W. Yang, S. Lee, H. C. Kwon, J. Tan, H. Lee, J. Park, Y. Oh, H. Choi and J. Moon, *ACS Nano*, 2018, **12**, 11088–11097, DOI: 10.1021/acsnano.8b05446.
8 P. R. Narangari, J. D. Butson, H. H. Tan, C. Jagadish and S. Karuturi, *Nano Lett.*, 2021, **21**, 6967–6974, DOI: 10.1021/acs.nanolett.1c02205.
9 N. Guijarro, M. S. Prevot and K. Sivula, *J. Phys. Chem. Lett.*, 2014, **5**, 3902–3908, DOI: 10.1021/jz501996s.
10 D. Kang, J. C. Hill, Y. Park and K.-S. Choi, *Chem. Mater.*, 2016, **28**, 4331–4340, DOI: 10.1021/acs.chemmater.6b01294.
11 S. P. Berglund, F. F. Abdi, P. Bogdanoff, A. Chemseddine, D. Friedrich and R. van de Krol, *Chem. Mater.*, 2016, **28**, 4231–4242, DOI: 10.1021/acs.chemmater.6b00830.
12 Y. Xu, J. Jian, F. Li, W. Liu, L. Jia and H. Wang, *J. Mater. Chem. A*, 2019, **7**, 21997–22004, DOI: 10.1039/c9ta07892d.
13 S. Wei, N. Xu, F. Li, X. Long, Y. Hu, L. Gao, C. Wang, S. Li, J. Ma and J. Jin, *ChemElectroChem*, 2019, **6**, 3367–3374, DOI: 10.1002/celc.201900714.

14 N. W. Kim, B. U. Choi, H. Yu, S. Ryu and J. Oh, *Opt. Express*, 2019, **27**, A171–A183, DOI: 10.1364/OE.27.00A171.
15 T. Chtouki, M. El Mrabet, A. Tarbi, I. Goncharova and H. Erguig, *Opt. Mater.*, 2021, **118**, 111294, DOI: 10.1016/j.optmat.2021.111294.
16 J. Yu, W. Han, A. A. Suleiman, S. Han, N. Miao and F. C. Ling, *Small Methods*, 2024, **8**, 2301282, DOI: 10.1002/smtd.202301282.
17 J. Lee, H. Yoon, S. Kim, S. Seo, J. Song, B. U. Choi, S. Y. Choi, H. Park, S. Ryu, J. Oh and S. Lee, *Chem. Commun.*, 2019, **55**, 12447–12450, DOI: 10.1039/c9cc06092h.
18 R. Garg, S. Gonuguntla, S. Sk, M. S. Iqbal, A. O. Dada, U. Pal and M. Ahmadipour, *Adv. Colloid Interface Sci.*, 2024, **330**, 103203, DOI: 10.1016/j.cis.2024.103203.
19 B. Duployer, C. Tenailleau, Y. Thimont, P. Lenormand, A. Barnabé and L. Presmanes, *Mater. Res. Bull.*, 2020, **130**, 110940, DOI: 10.1016/j.materresbull.2020.110940.
20 S. Shahidi, B. Moazzenchi and M. Ghoranneviss, *Eur. Phys. J.: Appl. Phys.*, 2015, **71**, 31302, DOI: 10.1051/epjap/2015140439.
21 B. Meena, M. Kumar, R. K. Hocking, S. Juodkazis, V. Biju, P. Subramanyam and C. Subrahmanyam, *Energy Fuels*, 2023, **37**, 14280–14289, DOI: 10.1021/acs.energyfuels.3c00731.
22 F. C. Krebs, *Sol. Energy Mater. Sol. Cells*, 2009, **93**, 394–412, DOI: 10.1016/j.solmat.2008.10.004.
23 F. Wang, A. Chemseddine, F. F. Abdi, R. van de Krol and S. P. Berglund, *J. Mater. Chem. A*, 2017, **5**, 12838–12847, DOI: 10.1039/c7ta03009f.
24 D. Perednis and L. J. Gauckler, *J. Electroceram.*, 2005, **14**, 103–111, DOI: 10.1007/s10832-005-0870-x.
25 T. H. V. Nguyen, C.-H. Wu, S.-Y. Lin and C.-Y. Lin, *J. Taiwan Inst. Chem. Eng.*, 2019, **95**, 241–251, DOI: 10.1016/j.jtice.2018.07.010.
26 C.-Y. Lin, S.-Y. Lin, M.-C. Tsai and C.-H. Wu, *Sustainable Energy Fuels*, 2020, **4**, 625–632, DOI: 10.1039/c9se00558g.
27 N. T. Hahn, V. C. Holmberg, B. A. Korgel and C. B. Mullins, *J. Phys. Chem. C*, 2012, **116**, 6459–6466, DOI: 10.1021/jp210130v.
28 E. Kalinina and E. Pikalova, *Materials*, 2021, **14**, 5584, DOI: 10.3390/ma14195584.
29 Y. Nakabayashi, M. Nishikawa and Y. Nosaka, *Electrochim. Acta*, 2014, **125**, 191–198, DOI: 10.1016/j.electacta.2014.01.088.
30 A. Al-Osta, B. S. Samer, U. T. Nakate, V. V. Jadhav and R. S. Mane, *Microelectron. Eng.*, 2020, **229**, 111359, DOI: 10.1016/j.mee.2020.111359.
31 M. G. Weldehans, T. T. K. Ngan, T. T. Salunkhe and I. T. Kim, *J. Mater. Chem. A*, 2025, **14**, 1601–1615, DOI: 10.1039/d5ta07895d.
32 H.-S. Kim, R. Verma, J. Kim and C.-J. Park, *ACS Sustainable Chem. Eng.*, 2020, **8**, 11123–11132, DOI: 10.1021/acssuschemeng.0c01513.
33 S. M. Paradine, *Tetrahedron*, 2025, 184, DOI: 10.1016/j.tet.2025.134781.
34 D. Piecha, J. Kapusta-Kołodziej, M. M. Marzec, K. Sokołowski, M. Kozieł and A. Brzózka, *Appl. Surf. Sci.*, 2025, **713**, 164330, DOI: 10.1016/j.apsusc.2025.164330.
35 T. Wu, J. Kim, Y. H. Choa and N. V. Myung, *Front. Chem.*, 2025, **13**, 1635084, DOI: 10.3389/fchem.2025.1635084.
36 M. Alhabradi, S. Nundy, A. Ghosh and A. A. Tahir, *ACS Omega*, 2022, **7**, 28396–28407, DOI: 10.1021/acsomega.2c02996.
37 M. Alruwaili, A. Roy, S. Nundy and A. A. Tahir, *RSC Adv.*, 2022, **12**, 34640–34651, DOI: 10.1039/d2ra05894d.
38 L. Zhao, X. Wang and Z. Liu, *Appl. Phys. A: Mater. Sci. Process.*, 2018, **124**, 836, DOI: 10.1007/s00339-018-2262-5.
39 J. Lee, H. Yoon, K. S. Choi, S. Kim, S. Seo, J. Song, B. U. Choi, J. Ryu, S. Ryu, J. Oh, C. Jeon and S. Lee, *Small*, 2020, **16**, e2002429, DOI: 10.1002/smll.202002429.
40 K.-H. Park and M. Dhayal, *RSC Adv.*, 2015, **5**, 33503–33514, DOI: 10.1039/c4ra15704d.
41 K. D. Malviya, H. Dotan, D. Shlenkevich, A. Tsyganok, H. Mor and A. Rothschild, *J. Mater. Chem. A*, 2016, **4**, 3091–3099, DOI: 10.1039/c5ta07095c.
42 O. Ait Layachi, A. Moujib and E. M. Khoumri, *Electroanal.*, 2024, 36, DOI: 10.1002/elan.202400115.
43 J. Lin, M. Kilani, M. Baharfar, R. Wang and G. Mao, *Nanoscale*, 2024, **16**, 19564–19588, DOI: 10.1039/d4nr02389g.
44 X. Wang, W. Liu, C. Wang, S. Zhang, M. Ding and X. Xu, *Sens. Actuators, B*, 2021, **344**, 130190, DOI: 10.1016/j.snb.2021.130190.
45 F. Wang, H. Yang and Y. Zhang, *Mater. Sci. Semicond. Process.*, 2018, **73**, 58–66, DOI: 10.1016/j.mssp.2017.09.029.
46 J. Wang, L. Tang, G. Zeng, Y. Liu, Y. Zhou, Y. Deng, J. Wang and B. Peng, *ACS Sustainable Chem. Eng.*, 2016, **5**, 1062–1072, DOI: 10.1021/acssuschemeng.6b02351.
47 S. Yu, H. Huang, F. Dong, M. Li, N. Tian, T. Zhang and Y. Zhang, *ACS Appl. Mater. Interfaces*, 2015, **7**, 27925–27933, DOI: 10.1021/acsami.5b09994.
48 J. Ghijsen, L. H. Tjeng, J. van Elp, H. Eskes, J. Westerink, G. A. Sawatzky and M. T. Czyzyk, *Phys. Rev. B: Condens. Matter Mater. Phys.*, 1988, **38**, 11322–11330, DOI: 10.1103/physrevb.38.11322.
49 HarwellXPS, HARWEllXPS GURU, https://www.harwellxps.guru/xpskb/copper/#1755794343725-850aaad2-863d, (accessed 10th September, 2025).
50 M. C. Biesinger, *Surf. Interface Anal.*, 2017, **49**, 1325–1334, DOI: 10.1002/sia.6239.
51 M. C. Biesinger, L. W. M. Lau, A. R. Gerson and R. S. C. Smart, *Appl. Surf. Sci.*, 2010, **257**, 887–898, DOI: 10.1016/j.apsusc.2010.07.086.
52 L. Qu, R. Tan, A. Sivanantham, M. J. Kang, Y. J. Jeong, D. H. Seo, S. Kim and I. S. Cho, *J. Energy Chem.*, 2022, **71**, 201–209, DOI: 10.1016/j.jechem.2022.03.013.
53 S. Sharma and N. Khare, *Colloid Polym. Sci.*, 2018, **296**, 1479–1489, DOI: 10.1007/s00396-018-4362-3.
54 F. Wang, W. Septina, A. Chemseddine, F. F. Abdi, D. Friedrich, P. Bogdanoff, R. van de Krol, S. D. Tilley and S. P. Berglund, *J. Am. Chem. Soc.*, 2017, **139**, 15094–15103, DOI: 10.1021/jacs.7b07847.
55 M. Li, X. Tian, X. Zou, X. Han, C. Du and B. Shan, *Int. J. Hydrog. Energy*, 2020, **45**, 15121–15128, DOI: 10.1016/j.ijhydene.2020.03.242.
56 N. Hoang Lam, N. Tam Nguyen Truong, K.-S. Ahn, Y. Jo, S. Beom Kang, N. Huu Hieu, S. F. Shaikh, C.-D. Kim, M. Lee and J. Hak Jung, *FlatChem*, 2024, **43**, 100600, DOI: 10.1016/j.flatc.2023.100600.
57 S. Huang, G. Wang, J. Liu, C. Du and Y. Su, *ChemCatChem*, 2020, **12**, 4431–4445, DOI: 10.1002/cctc.202000634.

58 A. Kudo and Y. Miseki, *Chem. Soc. Rev.*, 2009, **38**, 253–278, DOI: 10.1039/b800489g.
59 M. Mouanga, L. Ricq and P. Berçot, *J. Appl. Electrochem.*, 2007, **38**, 231–238, DOI: 10.1007/s10800-007-9430-1.
60 S. Survilienė, O. Nivinskienė, A. Češunienė and A. Selskis, *J. Appl. Electrochem.*, 2006, **36**, 649–654, DOI: 10.1007/s10800-005-9105-8.
61 W. Xue, J. Tian, X. Hu, J. Fan, T. Sun and E. Liu, *Chem. Eng. J.*, 2022, **443**, 136427, DOI: 10.1016/j.cej.2022.136427.
62 S. Zhang, M. Rohloff, O. Kasian, A. M. Mingers, K. J. J. Mayrhofer, A. Fischer, C. Scheu and S. Cherevko, *J. Phys. Chem. C*, 2019, **123**, 23410–23418, DOI: 10.1021/acs.jpcc.9b07220.
63 M. G. De Chialvo, J. Zerbino, S. Marchiano and A. Arvia, *J. Appl. Electrochem.*, 1986, **16**, 517–526, DOI: 10.1007/BF01006847.
64 H. Khan, M.-J. Kim, P. Balasubramanian, M.-J. Jung and S.-H. Kwon, *Cell Rep. Phys. Sci.*, 2023, **4**, 101652, DOI: 10.1016/j.xcrp.2023.101652.